



High-resolution optoacoustic imaging of tissue responses to vascular-targeted therapies

Katja Haedicke¹, Lilach Agemy², Murad Omar^{3,4}, Andrei Berezhnoi^{3,4}, Sheryl Roberts⁵, Camila Longo-Machado⁵, Magdalena Skubal¹, Karan Nagar⁶, Hsiao-Ting Hsu⁵, Kwanghee Kim⁶, Thomas Reiner^{5,7}, Jonathan Coleman^{5,8}, Vasilis Ntziachristos^{3,4}, Avigdor Scherz² and Jan Grimm^{1,5,7,9} ✉

The monitoring of vascular-targeted therapies using magnetic resonance imaging, computed tomography or ultrasound is limited by their insufficient spatial resolution. Here, by taking advantage of the intrinsic optical properties of haemoglobin, we show that raster-scanning optoacoustic mesoscopy (RSOM) provides high-resolution images of the tumour vasculature and of the surrounding tissue, and that the detection of a wide range of ultrasound bandwidths enables the distinction of vessels of differing size, providing detailed insights into the vascular responses to vascular-targeted therapy. Using RSOM to examine the responses to vascular-targeted photodynamic therapy in mice with subcutaneous xenografts, we observed a substantial and immediate occlusion of the tumour vessels followed by haemorrhage within the tissue and the eventual collapse of the entire vasculature. Using dual-wavelength RSOM, which distinguishes oxyhaemoglobin from deoxyhaemoglobin, we observed an increase in oxygenation of the entire tumour volume immediately after the application of the therapy, and a second wave of oxygen reperfusion approximately 24 h thereafter. We also show that RSOM enables the quantification of differences in neoangiogenesis that predict treatment efficacy.

With the intent of depriving cancer cells of nutrients and oxygen and reducing metastasis, many cancer therapies have been developed to either arrest existing tumour perfusion (anti-vascular) or prevent neovascularization (anti-angiogenic). Although anti-angiogenic drugs, such as bevacizumab, have shown some promise, their efficacy is limited by the development of therapeutic resistance, as well as by ensuing tumour hypoxia and, therefore, impairing subsequent drug delivery, which might explain the disappointing overall survival after anti-angiogenic therapy¹. These unexpected effects highlight the need for a means of monitoring the effects of anti-vascular and anti-angiogenic therapy *in vivo* over time.

Until recently, the therapeutic response of tumour vessels could be examined either only for a small area or only at a low resolution. Available methods include intravital microscopy, which is an invasive procedure with a small field of view; real-time laser speckle imaging, which is limited to a small tumour volume; or low-resolution non-invasive modalities such as blood oxygenation level-dependent (BOLD) magnetic resonance imaging (MRI), diffuse optical tomography to follow, for example, the response to chemotherapy in breast cancer; bioluminescence imaging of luciferase-transfected tumours; and ultrasound imaging of anti-vascular therapy-induced tumour necrosis^{2–7}. More recently, anti-vascular therapeutic effects have been monitored using conventional multispectral optoacoustic tomography (MSOT), a method that offers views of the entire tumour but also at only a low resolution that does not allow the depiction of vascular structures⁸. Furthermore,

a 640 nm photoacoustic scanner was used to observe the pharmacodynamic response of a chemotherapeutic agent; however, this observation also showed only longitudinal changes at low resolution, detecting only larger vessels surrounding the tumour tissue and did not use broad ultrasound bandwidth or dual-spectral imaging to resolve different states of oxygenation⁹. Thus, none of these modalities enables analysis of the vascular bed with simultaneous quantification of changes in the level of oxygenation at such high resolution as presented here using the dual-wavelength modality. Importantly, none of these modalities provided predictive parameters for tumour response or enabled the detection of early or late biological effects.

By contrast, the imaging modality of raster-scanning optoacoustic mesoscopy (RSOM) provides non-invasive high-resolution images of the entire tumour vasculature and surrounding tissue vessels. While MSOT uses a 5 MHz tomographic approach for signal detection, in which the whole body of the animal can be imaged using a multispectral 10 Hz laser at resolutions of about 160 μm ¹⁰, RSOM uses a raster-scanning approach with fast nanosecond-pulsed (up to 2 kHz) laser excitation of tissues and tumours and a 50 MHz single-element transducer. Absorption of the transient light energy by tissue chromophores, such as haemoglobin contained within blood vessels, generates ultrasound signals through short thermoelastic expansion of the excited molecules¹¹. Ultra-wide bandwidth, high-frequency detectors and narrow laser pulses enable the generation of high-resolution optical absorption images, revealing sub-millimetre fine vascular structures up to several millimetres in depth¹².

¹Molecular Pharmacology Program, Memorial Sloan Kettering Cancer Center, New York, NY, USA. ²Department of Plant and Environmental Sciences, Weizmann Institute of Science, Rehovot, Israel. ³Chair for Biological Imaging, Technical University Munich, Munich, Germany. ⁴Institute for Biological and Medical Imaging, Helmholtz Center Munich, Neuherberg, Germany. ⁵Department of Radiology, Memorial Sloan Kettering Cancer Center, New York, NY, USA. ⁶Urology Service, Department of Surgery, Memorial Sloan Kettering Cancer Center, New York, NY, USA. ⁷Department of Radiology, Weill Cornell Medical College, New York, NY, USA. ⁸Department of Urology, Weill Cornell Medical College, New York, NY, USA. ⁹Pharmacology Program, Weill Cornell Medical College, New York, NY, USA. ✉e-mail: grimmj@mskcc.org

The first application of RSOM was to resolve the vasculature of a melanoma tumour and the vascular bed surrounding the tumour tissue *in vivo* over time with an axial and lateral resolution of up to 5 μm and 20 μm , respectively¹³, although melanin in the tumour limited the signal penetration. RSOM has also been used to image the whole body of zebrafish using a 360° multi-orientation approach¹⁴. In humans, RSOM has been demonstrated to distinguish between individual layers of skin and to depict a benign nevus^{15,16}, to reveal simple hyperthermia effects¹⁷, and to detect pathophysiological biomarkers of psoriasis and inflammation¹². Moreover, dual-spectral RSOM imaging has been shown to discern melanin and blood oxygenation in normal human skin¹⁸. However, to date, RSOM has been used only to generate static images of benign events and has never been used in any oncology studies or to monitor dynamic changes.

Here, we explored RSOM and dual-wavelength RSOM as a non-invasive and high-resolution imaging tool to characterize tumour vessels and to quantify the dynamic response to an anti-vascular cancer therapy at the mesoscopic level in several mouse models of cancer. Particularly, we aimed to demonstrate the ability of RSOM to visualize the formation of blood vessels at high resolution and to evaluate response of tumour vessels to pharmacological stimuli over only a few minutes. Finally, we monitored the outcome of vascular-targeted photodynamic therapy (VTP) with padeliporfin (Tookad soluble)^{19,20}, a palladium-bacteriochlorophyll derivative photosensitizer that was recently clinically approved for non-thermal ablation of early stage low-risk prostate cancer following clinical trials in Europe^{21–23}. Treatment is achieved by tail-vein infusion of padeliporfin, after which the tumour area is selectively illuminated using a 753 nm laser, locally exciting padeliporfin in the bloodstream¹⁹. This induces the generation of oxygen radicals²⁴ from blood-borne oxygen, leading to irreversible vascular occlusion followed by tumour cell death and ultimately ablation of the tumour. One of the major advantages of padeliporfin is its fast clearance from the bloodstream, reducing unwanted side effects of skin photosensitivity or accumulation in other organs¹⁹.

We examined the correlation between the vascular response and the therapeutic efficacy of VTP using padeliporfin. We evaluated both immediate short-term changes within single blood vessels, and long-term effects and alterations across the whole tumour vascular bed and its surrounding tissue over several days. Finally, we aimed to identify RSOM-derived parameters that could be used to predict treatment response and shed light on the mechanism of action of VTP. The integration of a second pulsed laser into the RSOM system enabled us to evaluate oxyhaemoglobin and deoxyhaemoglobin, providing the opportunity to image oxygen distribution within and around the tumour after therapy.

Results

RSOM imaging of tumour vascular growth and brain vasculature. We first evaluated RSOM as a method for monitoring the tumour vascular bed during the growth of subcutaneous CT26 colon carcinoma tumours. Separating ultrasound signals into lower (5–25 MHz) and higher (25–80 MHz) frequencies revealed a complex network of tortuous tumour vessels, in which larger vessels (coded as red) branch out into smaller vessels (coded as green; Table 1, Fig. 1b). Merging both sub-bands revealed an overlap of high and low frequencies (orange to yellow in all following images), indicating that several vessels emit in both frequency bands and are of intermediate size, which was also observed by scanning through different depths of the tumour (Fig. 1c). Reconstructing a three-dimensional (3D) image of the tumour revealed the 3D vascular network within the tumour in detail (Fig. 1c, bottom; Supplementary Video 1). Sequential RSOM images of CT26 tumour growth showed that an intricate vascular network of smaller vessels developed as early as 3 d after implantation (Fig. 1d). At around day 8, tumour

Table 1 | Biological interpretation of the RSOM image features

| RSOM image feature | Biological interpretation |
|---|--|
| Connected network of homogenous signals | Blood vessels in tumour and skin |
| Green-coded vascular structures | High ultrasound frequencies (25–80 MHz) denoting smaller blood vessels with a ~15–48 μm diameter ^a |
| Red-coded vascular structures | Low ultrasound frequencies (5–25 MHz) denoting larger blood vessels with ~48–240 μm diameter ^b |
| Dotted yellow-coded structures | Clotted blood emitting a wide range of ultrasound frequencies of 5–80 MHz |
| Loss of signal over time to no signal | Occluded or destructed blood vessels |
| Homogenous red-coded signal of larger extent, not adhering to vascular structures | Haemorrhage into the tumour tissue from disrupted blood vessels |
| Extended area of irregular signal intensity without vascular structures | Necrotic tissue |

^aMainly capillaries and capillary-like vessels. ^bMainly feeding arteries/arterioles as well as draining veins/venules.

vessels appeared to be more mature, as the proportion of smaller vessels decreased, and larger vessels formed. At day 17 after tumour implantation, a branched and chaotic vascular system became predominant. These analyses demonstrate that RSOM enables the visualization of changes in tumour vasculature over time at vessel-level resolution. Depth analysis revealed that vessels of up to approximately 2.5 mm deep in the tissue could be visualized under good conditions in a subcutaneous tumour; that is, smaller tumours can be scanned in their entirety.

RSOM was then applied to image a mouse brain through the intact skull as well as the exposed brain after removing the skullcap (Fig. 1e). Mainly bigger vessels were visible through the enclosed skull, whereas very fine structures and smaller vessels were visible in the exposed brain in both the dorsal as well as the lateral view of the brain. The main artery in the middle of the brain and smaller branches could be clearly detected. The lateral view showed the curvature of the brain and deeper blood vessels.

To date, *ex vivo* histological methods have been used extensively to analyse blood vasculature. Although histology is a powerful technique, it requires multiple laborious steps to clear the tissue to even see vessels, including cryo-sectioning, staining, clearing and scanning of multiple consecutive slides. However, RSOM is advantageous over histology in several ways—RSOM enables repeated *in vivo* tracking of tumour vasculature over time in the same animal; it can cover a wider imaging area (more than 4 \times) at higher depths without the need of image stitching. Artefacts from tissue fixing, cutting and staining are also not an issue. Multiplexing of frequency bands enables us to distinguish between small and larger vessels and adds greater accuracy to the way that we can use RSOM to observe and track vessels of interest. In contrast to intravital microscopy, no invasive measures such as window chambers are required that could exert an effect on the observed tissues.

Visualizing adrenaline- and endothelin-induced vasoconstriction. As a first step, intensity profiles were taken from blood vessels in a CT26 tumour to prove the detectable vessel diameter (half-maximum width of the profile) in RSOM (Supplementary Fig. 1a,b). From the sagittal view, vessels with a diameter of 20 μm could be

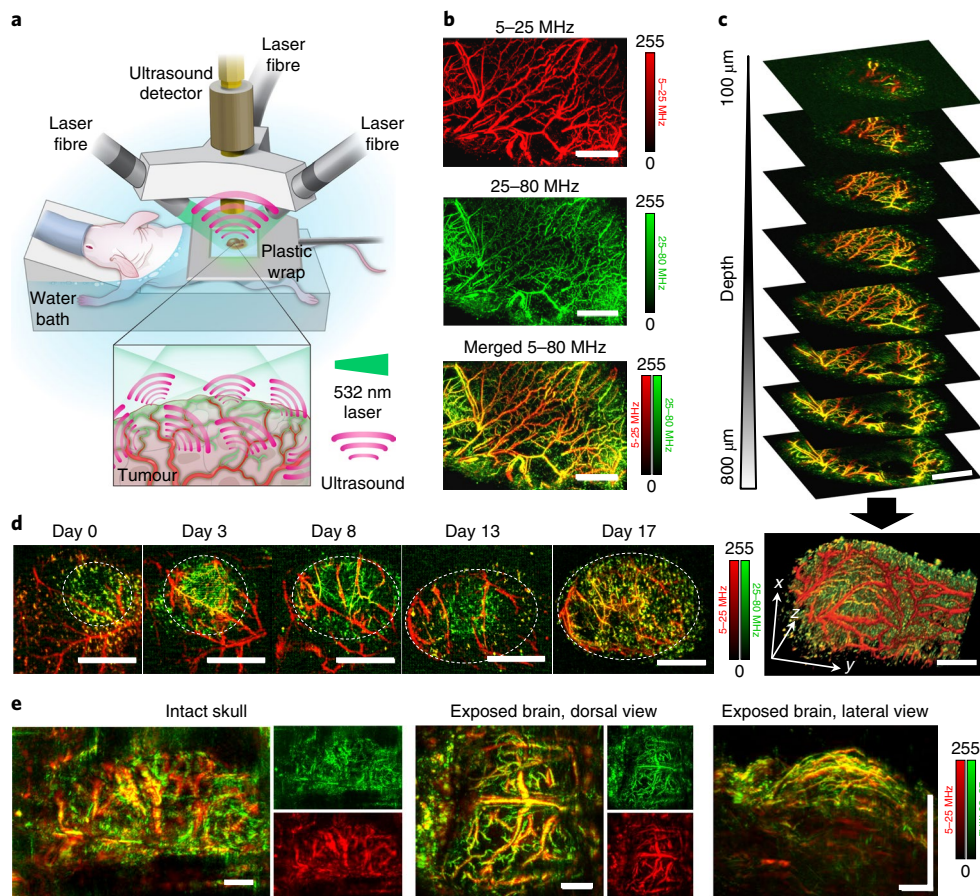


Fig. 1 | RSOM imaging of CT26 colon carcinoma tumours and mouse brain. **a**, Schematic of the experimental setup for the RSOM scanning of a mouse with a subcutaneous tumour. The animal is positioned in a water bath to couple the transducer to the animal. The three laser fibres coupled rigidly to the ultrasound detector scan in a raster pattern over the assigned field of view, which is stabilized using a thin plastic foil. After nanosecond-pulsed laser illumination at 532 nm, ultrasound waves are detected immediately. **b**, Optoacoustic MIP images of a CT26 tumour. Detected ultrasound frequencies were divided into two sub-bands to represent larger (5–25 MHz, red) and smaller (25–80 MHz, green) blood vessels. The merging of both frequency bands is represented by shades of yellow. Scale bars, 4 mm. **c**, Top, MIP images of slices through a CT26 tumour of up to 800 µm depth. Each image represents a 100 µm slice. Bottom, a 3D reconstruction of a CT26 tumour viewed from within the animal towards the skin. Scale bars, 4 mm. **d**, CT26 tumour growth over 17 d after implantation. Larger vessels (5–25 MHz) are indicated in red and smaller vessels (25–80 MHz) are indicated in green; merge/overlap of high- and low-frequency signals is indicated in yellow (the colour bar applies to all of the images in this Article unless specified otherwise). The white circle indicates the tumour area. Scale bars, 4 mm. **e**, RSOM MIP images of an intact mouse skull (the image shows half of the skull with skin removed) and an exposed brain after removing the skullcap (dorsal and lateral view). Scale bars, 1 mm. The major vessels can still be identified on the right side of the brain through the skull bone. Fig. 1a courtesy of the Memorial Sloan Kettering Cancer Center 2019.

detected. In the axial view, vessels with a diameter of 40 µm were visible. The different resolution is due to the detector design and that it has only one transducer element scanning from above along the skin surface.

To demonstrate that RSOM can identify small, early changes within the vascular network of a tumour, we imaged pharmacological vasoconstriction of individual vessels. At 1 min after injection of adrenaline, a reduction in the diameter of individual vessels within CT26 tumours was clearly discernible on enlarged maximum intensity projection (MIP) images (Fig. 2a). The ultrasound frequency emitted by several vessels changed from low (red) to high (green), consistent with a decrease in vessel width. At 5 min and 10 min after injection, tumour vessels began to dilate, as indicated by a return to a lower frequency signal (yellow/red). The same observations were made after injection of endothelin-1 (Fig. 2b)—clear vasoconstriction at 1 min after injection, apparent as emission of higher frequencies (green), and vasodilation (return to lower frequencies) within 5–10 min (Fig. 2b, insets). At 10 min after vasoconstriction using either agent, several new vessels appeared.

Quantification of the diameter of single tumour vessels in several animals over time confirmed an almost 50% decrease in vessel size at 1 min after injection of either adrenaline or endothelin-1, and that vessels returned to baseline diameter by 10 min after injection (Fig. 2c,d). Interestingly, normal vessels of the surrounding skin reacted differently, failing to contract at all, as visualized in RSOM MIP images (Supplementary Fig. 2a,b). A quantification of representative skin-vessel diameters in several animals confirmed this observation; vessel diameters remained nearly unchanged over time after injection of either vasoconstrictor agent (Supplementary Fig. 2c,d), which is probably species specific. The ability of RSOM to reveal changes at the level of individual vessels over time demonstrates the high sensitivity of this modality.

Monitoring the efficacy of VTP in CT26 tumours using RSOM.

VTP was performed by infusing the photosensitizer padeliporfin intravenously, followed by immediate laser illumination of the tumour, and the treatment effect was monitored over the next hour using RSOM imaging (Fig. 3a). Single-layer images through

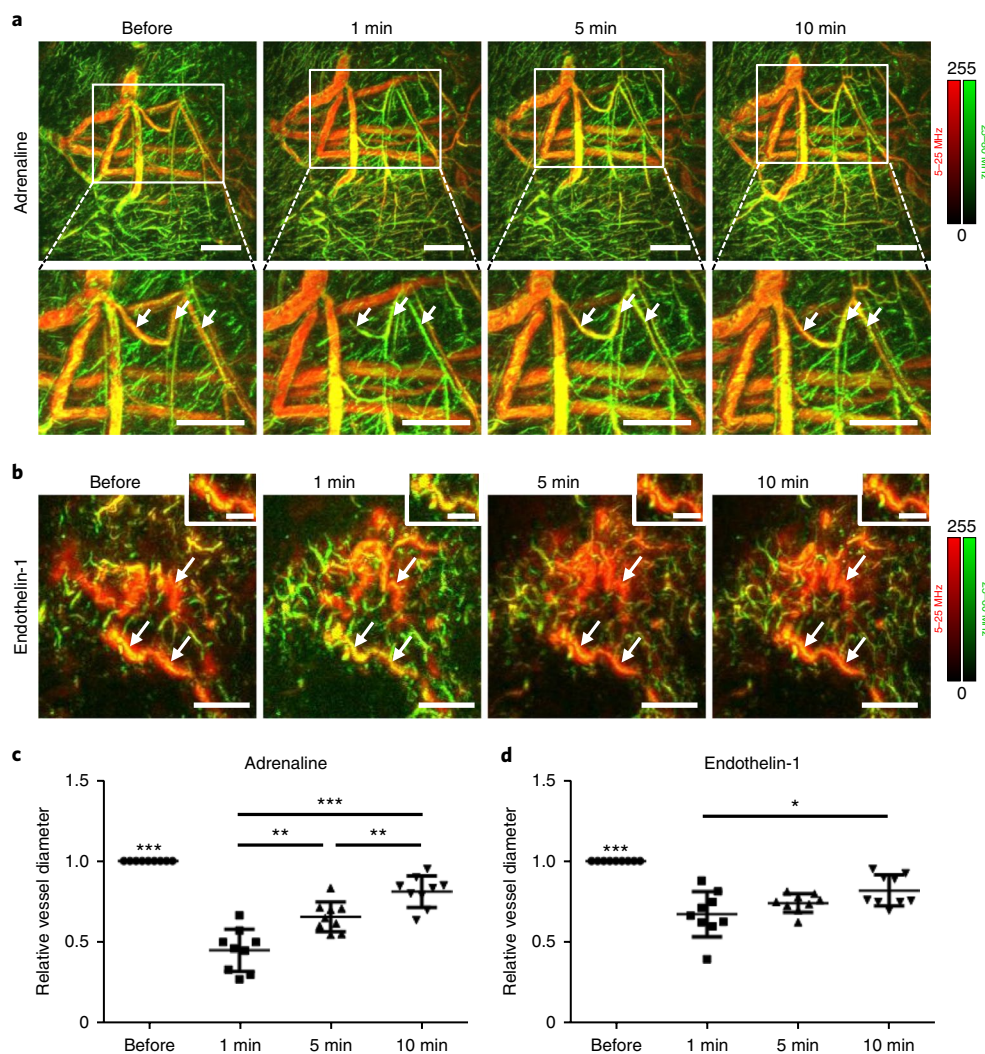


Fig. 2 | RSOM imaging of pharmacological vasoconstriction in CT26 tumours after injection of adrenaline or endothelin-1. **a**, MIP images of CT26 tumour vessels over the 10 min after injection of adrenaline. The arrows in the magnified images indicate vasoconstriction. Scale bars, 2 mm. **b**, MIP images of CT26 tumour vessels over the 10 min after injection of endothelin-1. Insets: changes in a single blood vessel over time. Scale bars, 1 mm and 0.5 mm for main images and insets, respectively. **c,d**, Relative vessel diameters from three different tumours ($n=3$ biological replicates) over the 10 min after injection of adrenaline (**c**) or endothelin-1 (**d**). Data are mean \pm s.d. of three mice. Data were compared using unpaired two-tailed Student's *t*-tests; *** $P < 0.0001$; ** $P = 0.0013$ for 1 min versus 5 min and $P = 0.0031$ for 5 min versus 10 min; * $P = 0.0195$.

varying depths of a small (diameter of <6 mm) low-vascularized CT26 tumour revealed distinct vascular events (Fig. 3b). In superficial tumour vessels (at a depth of $350 \mu\text{m}$ from the skin surface), VTP induced intravascular clotting, as indicated by denser optoacoustic signals. Vessels deeper inside the tumour (at a depth of $570 \mu\text{m}$ from the skin surface), which were clearly visible before VTP, occluded and disappeared within 10 min after illumination. As vessels lost integrity, haemorrhage became visible as an irregular red spot inside the tumour that was not confined to vascular architecture. Furthermore, clotting of smaller vessels was detected as more intense signals in the vascular pattern, especially at the tumour rim, reflecting the higher density of haemoglobin within blood clots. RSOM revealed blockage and destruction of the larger tumour-feeding skin vessels over time, which were visible as a decrease in signal. Quantitative analysis of the relative haemoglobin signal in RSOM images over time confirmed these observations (Fig. 3c).

After VTP treatment in larger (diameter of >6 mm) more vascularized CT26 tumours, RSOM clearly showed vascular constriction

followed by destruction of several blood vessels. Here, larger tumour vessels were occluded at 5 min after VTP (Fig. 4a). Single vessels could be followed throughout the progress of the effects of VTP. At 1 h, occlusion and disappearance of small vessels was pronounced and accompanied by slight haemorrhage, appearing as red spots within the RSOM images. Quantification of relative haemoglobin levels over time after VTP showed that the signal decreased within 5 min after VTP in both low- and high-frequency bands, reflecting the destruction of both larger and smaller vessels (Fig. 4b, left). The number of vessel fragments increased due to vessel breakage (Fig. 4b, right). Histological analysis corroborated these observations (Supplementary Fig. 3), revealing—at 1 h after VTP, damage to tumour tissue (haematoxylin and eosin (H&E))—massive destruction of tumour blood vessels (CD31) and apoptotic and necrotic cells (TUNEL), in contrast to the untreated control tumours, in which tumour tissue remained intact, with many vessels and no obvious dead cells. These analyses demonstrate the suitability of RSOM imaging for quantitative monitoring of rapid changes in tumour vasculature in real time.

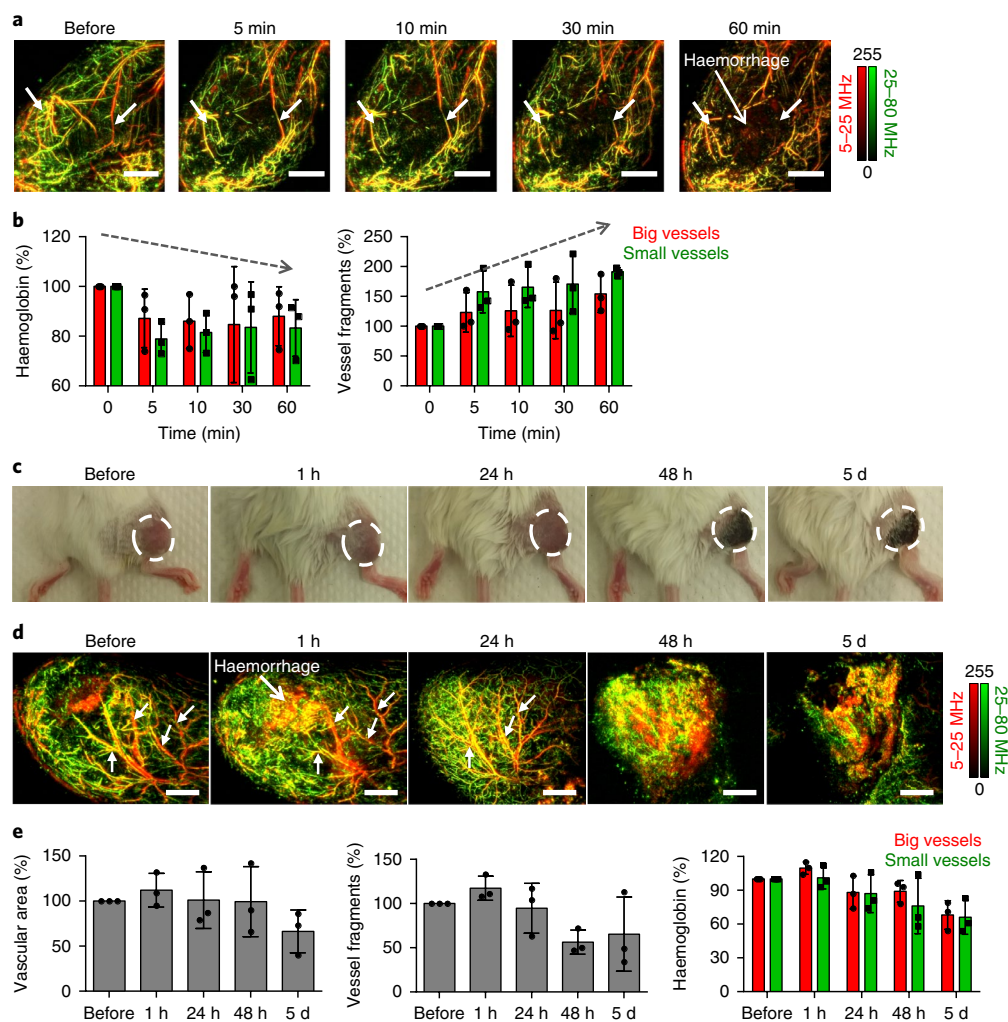


Fig. 4 | Short- and long-term longitudinal RSOM imaging of the effects of padeliporfin VTP in CT26 tumours. **a**, RSOM MIP images of a CT26 tumour after padeliporfin VTP over time. The arrows indicate the destruction of representative vessels and haemorrhage after 60 min. Scale bars, 2 mm. **b**, Quantitative analysis of the effect of VTP. The relative amount of haemoglobin and the number of vessel fragments were quantified in each frequency channel over time; $n=3$ biological replicates. Dashed black arrows show the trend of haemoglobin signal and vessel fragments. Data are mean \pm s.d. **c**, Photographs of a BALB/c mouse with a CT26 tumour in the right thigh over time up to 5 d after VTP treatment. The dark tissue reflects necrosis. The dotted circle indicates the tumour area. **d**, RSOM MIP images of the vascular network of a CT26 tumour over time for up to 5 d after padeliporfin VTP. The arrows follow individual vessels over time. Scale bars, 2 mm. **e**, Quantitative analysis of the relative vascular area (total signal), relative number of vessel fragments, and relative haemoglobin signal in the red (larger vessels) and green (smaller vessels) channels in CT26 tumours after VTP over time; $n=3$ biological replicates. Data are mean \pm s.d.

baseline), as presented in the 3D surface plots (Fig. 5b). The same effect was visible in the RSOM MIP images of the same tumour (Fig. 5c). A more detailed analysis revealed a temporary increase in oxygenated haemoglobin throughout the tumour 5 min after VTP (Fig. 6a), indicating rapid reperfusion. The oxygenation level then dropped, which is shown as a reduction of the red oxygenated area and an expansion of the blue deoxygenated area. Quantification of these images demonstrated a shift towards lower oxygenation values (into the blue end of the scale), from a mean value of 35,089 AU before VTP to 24,618 AU at 1 h after treatment (Fig. 5d). At 24 h after VTP, oxygenation of tumour vessels almost ceased (Fig. 6a), corroborated by clotting and necrosis (homogenous signal) observed in the 532 nm vascularization images (Fig. 6a, bottom). Quantification of relative oxygenation confirmed the patterns observed in the gradient images; an increase in oxygenation at 5 min after VTP was followed by a large decrease for up to 24 h (Fig. 6b). Thus, quantitative analysis of oxygenation levels using dual-wavelength RSOM enables

the examination of functional effects of anti-vascular therapies in real time.

RSOM imaging of varying degrees of tumour control by VTP.

We next sought to evaluate RSOM as a tool to predict treatment response. On the basis of their distinct cure rates at 15 d after VTP, we chose models of bladder cancer in which either UMUC3 or patient-derived 5637 cells were xenografted into mice; UMUC3 tumours were less effectively treated by padeliporfin VTP than the 5637 tumours. RSOM images of UMUC3 tumours showed more extensive neoangiogenesis compared with the 5637 tumours (Fig. 7a). Interestingly, as early as 1 h until 24 h after treatment, ischemic reperfusion of initially non-vascularized tumour tissue was apparent in the 5637 tumours (similar to CT26 tumours; Fig. 4d), but was minimal in UMUC3 tumours, in which mostly larger vessels deteriorated by 24 h. At 3 d after treatment, the vasculature of the 5637 tumours completely collapsed, and the periphery of the

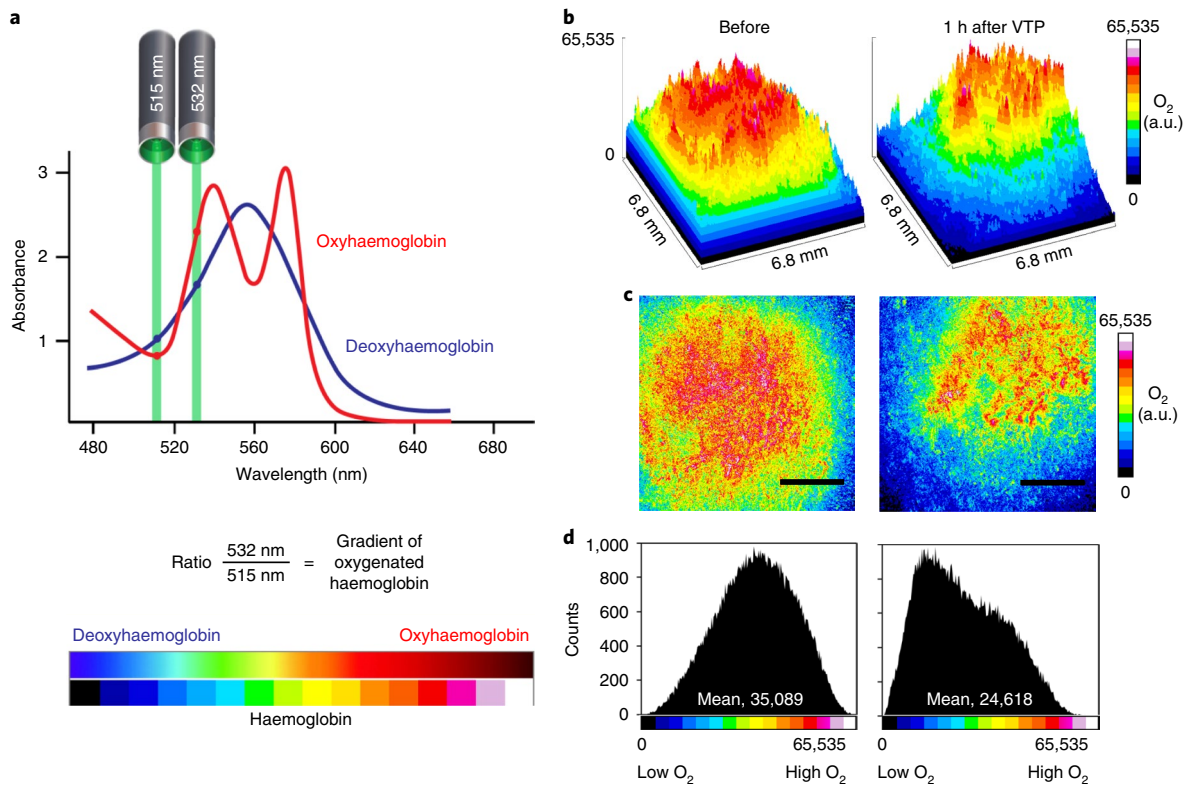


Fig. 5 | Dual-wavelength RSOM imaging before and 1 h after padeliporfin VTP to visualize tumour oxygenation. a, Absorbance spectra of oxyhaemoglobin (red) and deoxyhaemoglobin (blue). The green laser beams indicate the wavelengths that were used for dual-wavelength RSOM imaging. The ratio of the signal at 532 nm to 515 nm was used to calculate the gradient of oxygenated haemoglobin. The colour scales show the colour scheme used in the oxygenation images (black/blue indicate low oxygen; red/white indicate high oxygen). **b**, 3D surface plots of oxygenation before and 1 h after VTP. **c**, Dual-wavelength RSOM MIP images of relative tumour oxygenation before and 1 h after therapy. Scale bars, 2 mm. **d**, The distribution of the oxygenation values before and 1 h after VTP. Fig. 5a courtesy of the Memorial Sloan Kettering Cancer Center 2019.

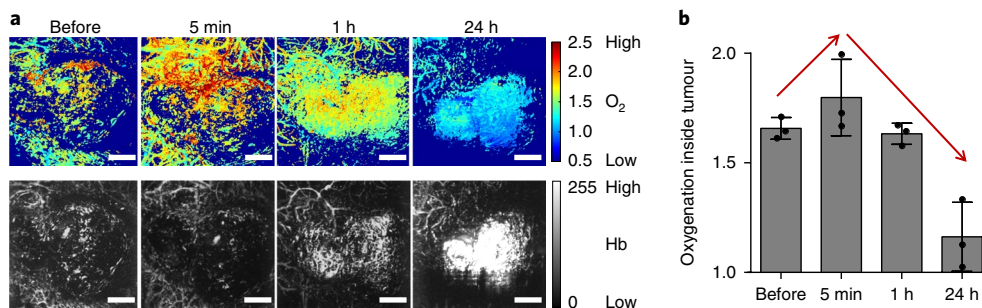


Fig. 6 | Dual-wavelength RSOM imaging of tumour oxygenation and vascularization in CT26 tumours over time after padeliporfin VTP. a, Dual-wavelength RSOM MIP images of the relative oxygenation levels in a CT26 tumour up to 24 h after padeliporfin VTP. Low oxygen (O_2) is indicated in blue and high oxygen is indicated in red. The greyscale images show corresponding RSOM MIPs of the tumour vasculature over time. Hb, haemoglobin signal. Scale bars, 2 mm. **b**, Quantitative analysis of the relative oxygenation in tumours over time after VTP. The red arrows show the trend of oxygenation changes over time; $n = 3$ biological replicates. Data are mean \pm s.d.

tumour was vessel-free; by contrast, UMUC3 tumours exhibited a necrotic tumour centre with regrowth of small new vessels at the outer edges. While the 5637 tumours lost all remaining vessels, UMUC3 tumours grew a new vascular network. Measurements of tumour volume in these two models confirmed these observations (Fig. 7b); the 5637 tumours shrank, whereas the UMUC3 tumours increased in volume after VTP. These findings were further substantiated by white-light photographs (Supplementary Fig. 5), which showed complete tumour necrosis and a scab after VTP in

the mice bearing 5637 tumours, and central necrosis with extensive neoangiogenesis and regrowth at the tumour rim at day 3, resulting in a larger tumour at day 14 after VTP in the mice bearing UMUC3 tumours.

Quantification of RSOM MIP images revealed clear differences in relative haemoglobin signal, vascular area and vessel fragments that were consistent with treatment effect (Fig. 7c). Although the relative haemoglobin signal remained fairly stable in both models for up to 24 h after VTP, with only a slight increase in the lower

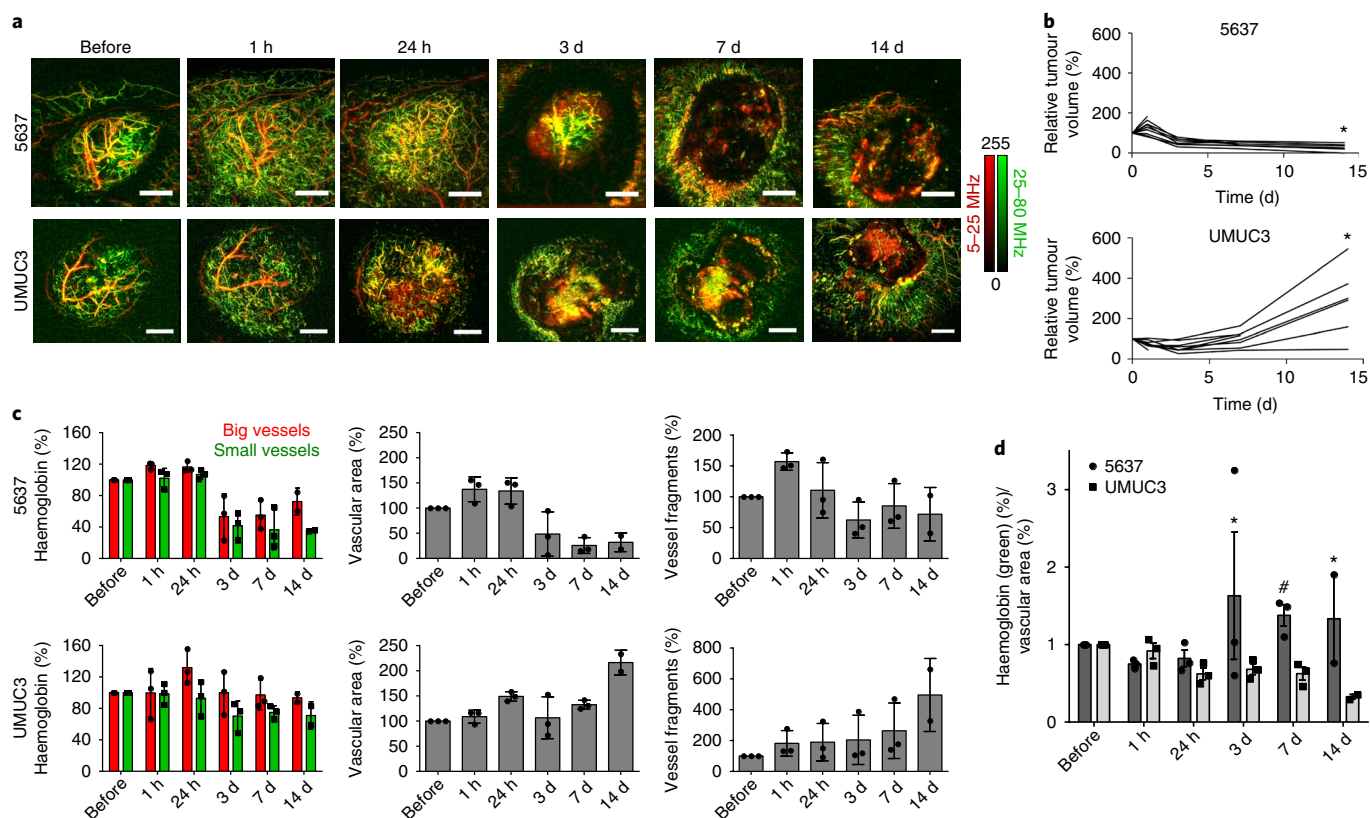


Fig. 7 | Comparison of vascularization between bladder tumours in which VTP is differentially effective. a, RSOM MIP images of the vasculature of 5637 and UMUC3 tumours over time up to 14 d after padeliporfin VTP. Scale bars, 2 mm. **b**, Relative tumour volume of 5637 and UMUC3 tumours over time after VTP. * $P=0.0114$ (at 14 d). **c**, Quantification of the relative haemoglobin levels in the low-frequency (red) and high-frequency (green) channels, relative vascular area, and relative number of vessel fragments in 5637 and UMUC3 tumours after VTP over time; $n=3$ (from before up to 7 d) and $n=2$ (14 d) biological replicates. Data are mean \pm s.d. **d**, The ratio of normalized haemoglobin (%) in the high-frequency (green) channel to normalized vascular area (%) in 5637 and UMUC3 tumours over time after VTP; $n=3$ (from before up to 7 d) and $n=2$ (14 d) biological replicates. Data are mean \pm s.e.m. Data were compared using unpaired two-tailed Student's *t*-tests; * $P=0.0239$ (3 d), * $P=0.047$ (14 d) and # $P=0.0096$ (7 d, if *P* is computed assuming inconsistent data scatter).

frequency channel in UMUC3 tumours due to haemorrhage, a decrease in signal was observed after only 3 d in the 5637 tumours (Fig. 7c, left). The haemoglobin signal remained low in the 5637 tumours, with a minimal increase in the lower frequency channel at day 14 due to necrosis and scarring. The overall vascular area in the 5637 tumours first increased slightly up to 24 h after VTP and decreased starting at 3 d (Fig. 7c, middle). By contrast, the vascular area in the UMUC3 tumours increased slightly up to day 7 after treatment, then increased at day 14 due to regrowth of new vessels. The number of vessel fragments increased in the 5637 tumours immediately after therapy due to vessel destruction and continued to decrease thereafter (Fig. 7c, right); by contrast, in UMUC3 tumours, the number of vessel fragments increased steadily due to the regrowth of new and more vessels, especially at 14 d after VTP. The ratio of high-frequency signal (small vessels) to the vascular area was much higher in the 5637 tumours compared with the UMUC3 tumours from day 3 onwards (Fig. 7d), at a time when the change in tumour volume was not yet apparent. Histopathology using H&E and CD31 staining corroborated these results (Supplementary Fig. 6), showing destruction of tissue and loss of vessels in the 5637 tumours, and regrowth of only slightly deteriorated tumour tissue and tumour blood vessels in the UMUC3 tumours. These findings suggest that RSOM may enable early differentiation of varying treatment effects of VTP and possibly other anti-vascular and anti-angiogenic treatments.

Discussion

We have described the application of RSOM for detailed imaging of temporal changes in tumour vascularization and oxygenation levels during and after vascular-targeted therapy. Together, our results demonstrate the ability of RSOM to reveal important aspects of the response of the tumour microenvironment to vascular-targeted treatments, clarify their mechanisms of action and improve treatment approaches. This imaging tool enables the non-invasive study of morphological and functional aspects of vessels at much deeper levels than optical microscopy and with high resolution, offering a considerable improvement over existing non-invasive approaches to image the vascular bed in considerable detail. Furthermore, in contrast to elaborate histology, temporal changes can be observed in the same animal.

We first evaluated the ability of RSOM to capture changes in tumour vascular morphology coincident with tumour growth over 17 d. RSOM images revealed an elaborate vascular network in CT26 tumours, which changed appearance as a function of time, revealing a progressive recession of smaller vessels with tumour growth and the development of a chaotic vascular system. RSOM therefore enables non-invasive high-resolution imaging of tumour neoangiogenesis, an advancement over previous techniques for imaging of tumour vascular growth, which were either low-resolution and non-invasive or high-resolution and invasive^{3,8}. Our study reveals vascular details within a tumour itself, as the previous investigation

was limited by the presence of strongly absorbing melanin within the tumour (a melanoma) and, therefore, mainly captured the vascular bed surrounding the tumour¹³, unable to penetrate into the tumour itself.

RSOM enabled us to follow relatively short temporal changes in the vascular bed of tumours and normal tissue, as demonstrated here using pharmacological manipulation with the administration of adrenaline or endothelin-1. RSOM consistently identified immediate changes in the diameter of individual CT26 tumour vessels, confirming their functional ability to respond to external stimuli. These findings demonstrate the high sensitivity of RSOM in capturing even minor alterations within a complex vascular network non-invasively. Although the exact biological mechanism behind the intriguing responsiveness of tumour vessels to vasoconstrictors and non-responsiveness of those in the surrounding skin requires further investigation, we surmise that it may result from recruitment of smooth muscle cells into the tumour, lowering their numbers in adjacent areas. Previous studies showed that pericytes are present in most tumour vessels, but show multiple abnormalities compared with those associated with normal capillaries, such as the overexpression of α -smooth muscle actin²⁶.

The ability of RSOM to follow changes in vessel diameter, as demonstrated here, provides an interesting opportunity to monitor vascular normalization in response to therapy. Such normalization is necessary to support the delivery of chemotherapeutics and radiotherapeutics to certain types of tumour^{27,28}. This effect has previously been imaged at very low resolution using daily MRI or positron emission tomography^{29,30}. The colour-coding system presented here, in which changes in vascular diameter are represented as changes in colour, enables real-time monitoring of such changes. The benefit of RSOM as a tool to help with the design and improvement of new and established treatments is also demonstrated by its ability to detect the immediate opening of alternative blood vessels. Both chemotherapy and radiotherapy are most effective in tumours that are homogeneously well vascularized, enabling the delivery of the drug or oxygen radical throughout the tumour. Thus, the intermittent blood flow, whereby different tumour domains may undergo perfusion at different time points, limits treatment to the perfused domains only. Monitoring changes in the perfusion of different tumour domains may enable better timed delivery of chemo- and/or radiotherapy and may account for the observed advantage of intermittently applied chemotherapies.

We demonstrated the ability of RSOM to provide a detailed picture of vascular events and the resulting changes in tissue oxygenation levels by monitoring the efficacy of VTP using the clinically approved photosensitizer padeliporfin in the CT26 tumour model. Changes in the functional parameters of tumours have recently been observed in tumours in response to padeliporfin treatment using MSOT, which offers views of the entire tumour, but at only low resolution⁸. Here we applied RSOM to elucidate responses at a resolution of a few micrometres at both short- and long-term intervals on the individual-vessel and whole-tumour levels. This had previously been possible only invasively using intravital fluorescence microscopy or, with certain limitations, using real-time laser speckle imaging with a dorsal window chamber in mice or using basic low-resolution modalities^{3,4,19,31,32}. However, none of these modalities enabled simultaneous quantification of changes in the tissue level of oxygenation at a high enough resolution to visualize individual vessels, as presented here, showing the use of RSOM to resolve the action mechanism of tumour treatment that involves vascular targeting and also whole-tissue response. Although previously published studies focused on the vascular events involved in tumour destruction, our study shed some light on the action mechanism of this tumour treatment. Here, the higher temporal and spatial resolutions of RSOM combined with multispectral analysis and wide bandwidth compared with other methods enabled us to

observe a transient oxygen reperfusion in the first few minutes after treatment. Notably, oxygen reperfusion is widely believed to be the major contributor to organ collapse in sepsis or stroke, all caused by ischemia–reperfusion injury rather than the ischemia alone. Moreover, the self-propagation of radicals into the tumour core that is necessary for VTP requires continuous provision of oxygen radicals enabled through the release of oxygen from haemoglobin into the tumour stroma, some of which could, at later timepoints, arise from haemorrhage into the tissues as a reservoir for oxygenated haemoglobin. Indeed, the observed temporal increase in oxygenation throughout the entire tumour tissue at 5 min after VTP and the slow decay observed long after the completion of vascular occlusion indicate that VTP leads to oxygen reperfusion outside vessels that is sustained for several hours, whereas the level of oxygen in the vessels drops. Combined with the observed overall ischemia, these findings suggest that VTP induces ischemia reperfusion injury. Although the vascular events are consistent with previous macroscopic observations performed by MSOT and other photoacoustic imaging systems^{8,33}, the observed oxygen reperfusion and predictive parameters provide an important insight into the VTP mechanism of action. Furthermore, tumour oxygenation has been identified as a prognostic indicator of treatment outcome in previous studies^{33,34}, highlighting the potential impact of such monitoring of physiological parameters on personalized treatments. However, a limitation of the previous studies is the poor spatial resolution of the images, as discussed above. Our current approach using RSOM represents a considerable advantage in technology by providing a means for high-resolution imaging of tumour blood vessels and oxygenation in a manner that could inform the delivery of light for treatment by mapping not only oxygen distribution. As a consequence, RSOM could be used to guide the delivery of adjuvant treatments to areas at high risk for recurrence.

To determine whether quantitative parameters that were derived from the features of RSOM images correlate with treatment success, we compared several changes in tumour vasculature after VTP in tumours grown from different cell lines (UMUC3 and 5637, both bladder carcinoma), which showed distinct cure rates after VTP (possibly due to differences in size and from increased angiogenesis). The profound differences in vascular changes between these tumour types indicate that RSOM parameters of vascular response may be useful for predicting the success of treatment before changes in tumour volume or tumour growth become apparent. Furthermore, specific differences between the effects in these tumours may provide insights into the biological mechanisms of the response. For example, the primary vascular response in all of the tumour types initially appears to be similar, including breakdown (occlusion) of feeding arteries and draining veins, haemorrhage and clot formation. However, regrowing tumours show evidence of recruiting new vessels from the periphery, whereas non-regrowing tumours do not. Thus, the vascular area of the regrowing tumours (including immediately adjacent tissue) is substantially larger, which could be used as an early indicator of regrowth. These findings demonstrate that RSOM provides a useful means to quantitatively examine the effects of modern vascular-targeted therapies, providing details regarding potential biological mechanisms that can be further investigated to improve therapeutic efficacy. In the future—and with the inclusion of several wavelengths—the applications of RSOM could potentially be extended beyond imaging not only blood vessels but also genetically modified tumour cells or other tissue processes as outlined with other, lower-resolution optoacoustic scanners³⁵. Furthermore, it might also be feasible in the future to use RSOM for endoscopic imaging, as was shown as a proof of concept in ex vivo swine phantoms³⁶, widening the applications, especially for orthotopic tumours. Our brain imaging data also suggest that RSOM has a future use for imaging orthotopic tumours in several organs, especially in preclinical research, substantially expanding the potential of RSOM.

One of the limitations of RSOM is the limited penetration depth, which is inherent to all high-resolution ultrasound detectors. However, in the context of our study, this was not a considerable limitation as we were able to prove that imaging of the tumour vessels near to the surface was sufficient to predict treatment outcomes for responding and non-responding tumours. Furthermore, the regrowth of vessels occurred starting from the surrounding tumour tissue (and not from the tumour core), which was depicted clearly using RSOM. Moreover, histology images, even from deeper inside the tumours, confirmed the features seen in the RSOM images.

In conclusion, we show that RSOM can be used to observe vascularity during tumour development and visualize critical changes in response to therapy. RSOM enables the detailed quantitative observation of morphological (vascularization) and physiological (oxygenation) features of tumour vascular dynamics that may inform the evaluation and development of new therapies and could be translated into a broad spectrum of other applications.

Methods

In vitro cell culture. Mouse colon carcinoma cells (CT26) were cultivated in RPMI 1640 medium (D-glucose, 2,000 mg l⁻¹; 10-040, Corning) supplemented with 2 mM L-glutamine (25030081, Thermo Fisher Scientific), 1 mM sodium pyruvate (25-000, Corning), 1% penicillin-streptomycin solution (30-002, Corning) and 10% fetal bovine serum (100-106, GeminiBio). Human urinary bladder grade II carcinoma cells (5637) from ATCC were cultured in RPMI 1640 medium with 10% fetal bovine serum, 2 mM L-glutamine and 1% penicillin-streptomycin solution. Human urinary bladder transitional cell carcinoma cells (UMUC3) from ATCC were grown in MEM medium (D-glucose, 1,000 mg l⁻¹; 10-010, Corning) with the same supplements as described for the 5637 cells. All of the cell lines were incubated at 37 °C in a 95% humidified atmosphere with 5% CO₂.

Animal models and tumour implantation. CT26 tumours were implanted into female BALB/c mice (Taconic, 6–8 weeks old) by subcutaneous injection of 1 × 10⁶ CT26 cells in 100 µl of 1:1 Matrigel (354234, Corning) and PBS (46-013, Corning) into the upper region of the thigh. 5637 and UMUC3 tumours were grafted into male NSG mice (NOD.Cg-Prkdc^{cid} Il2rg^{tm1Wjl}/Szj; Jackson Laboratory; 6–8 weeks old) by subcutaneously injecting 10 × 10⁶ or 3 × 10⁶ cells, respectively, in 100 µl of 1:1 Matrigel:medium into the right flank. Tumour growth was monitored over time; imaging was performed and therapy was delivered under 2% isoflurane inhalation anaesthesia (Forane isoflurane, NDC10019-360-60, Baxter) when implants reached sufficient size of at least 6 mm diameter (for CT26 tumours, approximately 14 d after implantation; for 5637, 33 d; and for UMUC3, 18 d). All of the mice were shaved with depilatory cream (hair removal lotion, Nair) before RSOM imaging to prevent light absorption and reduced image quality due to hair. During shaving and therapy application, the mice were placed on a warm cushion. Temperature was not monitored during the imaging sessions. All of the animal procedures were approved by the Institutional Animal Care and Use Committee (IACUC) and followed institutional and NIH guidelines.

RSOM. Optoacoustic images were generated using a prototype scanner and MATLAB-based software that were developed at the Helmholtz Centre in Munich as described previously^{33,37}. Specific RSOM scanner parameters are provided in Supplementary Table 1. In brief, the anaesthetized mouse was placed onto a bed and into a warmed water bath, with the tumour region under the water level and the head above the water level (Fig. 1a). The tumour was stabilized using thin plastic wrap to suppress breathing motion artefacts. Three laser fibres together with the 50 MHz spherically focused ultrasound detector were placed just above the tumour, and the designated area was scanned in a raster manner with 20 µm steps. The scan time for a field of view of 6 × 6 mm² was approximately 1.5 min and, for a larger field of view of 10 × 10 mm², about 4 min. During scanning, the tissue was illuminated using a nanosecond-pulsed 532 nm laser, which excites haemoglobin. The generated ultrasound signals were detected at a bandwidth of 5–80 MHz. The signals were subsequently amplified and digitized. During image reconstruction, 532 nm laser-induced signals were separated into lower (5–25 MHz, red) and higher (25–80 MHz, green) frequencies to distinguish larger (diameter of 48–240 µm) and smaller (diameter of 15–48 µm) vessels, respectively. This bandwidth separation was performed for all of the images using the exact same method by using the same frequency ranges, meaning that larger (red encoded) and smaller (green encoded) vessels represent the same size range throughout the whole study, including over time after treatment. For clarity of the figures, the colour bar is shown in Fig. 1; this colour bar applies to all other images unless specified otherwise. The dependency of detected frequency from vessel size can be calculated using the formula $f_c \approx 0.8c/d$ where f_c is the centre frequency, c represents the speed of sound with 1,500 m s⁻¹ and d is the diameter of the vessel³⁸. The images were processed using the Hilbert transform (assuming a speed of

sound of 1,540 m s⁻¹) along the depth as well as a Median and Wiener filter. Unless otherwise specified, images represent the MIP of the 3D volume, seen from above the tumour, as an RGB image (scaled always from 0 to 255) merging the low (red) and high (green) frequencies. Structures emitting frequencies in both frequency bands appear in orange to yellow colour in the images. A list of the specific features of the RSOM images and their biological interpretations is provided in Table 1.

For dual-wavelength RSOM to discriminate between oxyhaemoglobin and deoxyhaemoglobin, a second laser with a wavelength of 515 nm was added. Images were acquired for both wavelengths simultaneously and the corresponding data for each wavelength were separated before reconstruction. The detected ultrasound bandwidth for this approach was 10–100 MHz. The ratio of the signals at 532 nm to signals at 515 nm was used to calculate the relative gradient of oxygenated haemoglobin.

RSOM imaging of CT26 tumour vascular growth over time. CT26 tumours were implanted as described above. Before imaging, the tumour area and its immediate surroundings were shaved to reduce imaging artefacts. The tumour area was imaged using RSOM immediately after tumour implantation (day 0) and at days 3, 8, 13 and 17 after inoculation to assess the vascular changes that accompanied tumour growth.

Craniotomy and brain imaging. Under isoflurane anaesthesia, the mouse was placed into a stereotaxic frame, over a surgery warmer bed, and its head was firmly secured using ear bars. Meloxicam (5 mg kg⁻¹; 6451603845, Henry Schein Animal Health) was administered subcutaneously to prevent an inflammatory response. All of the surgical instruments were presterilized. The skin over the top of the skull was removed using scissors that were sterilized with ethanol, starting with a horizontal cut all along the base of the head followed by two cuts in the rostral direction, almost reaching the eyelids, and then two oblique cuts that converged at the midline. A drop of 2% lidocaine solution (S1357, Selleckchem) was applied pre-emptively onto the periosteum to avoid any pain. With a scalpel, the periosteum was retracted to the edges of the skull. The musculature at the back of the neck was also slightly retracted. The animal was imaged with intact skull in the RSOM. To create the cranial window, first a circle of about 7 mm in diameter was 'drawn' gently using a stereotaxic drill. After slight drilling, 2% lidocaine solution was applied again onto the skull surface. The drilling was stopped when a very thin layer of bone remained. Under a drop of saline and taking advantage of the bone trabeculae—the spongy structure of the bone—the craniotomy was lifted away from the skull using very-thin-tip forceps. The saline is important because it helps to lift up the skull and prevent bleeding of the dura. Gelfoam (NC9841478, Pfizer) that had been soaked in saline was applied to the dura mater to stop any small bleeding that sometimes occurs when the skull is removed. With the open skull, the mouse was placed back onto the bed of the RSOM. Using a sterile cotton swap, any excess saline was removed, and a generous amount of clear ultrasound gel (03-08, Parker Laboratories) was applied on top of the exposed brain. All of the mice were euthanized shortly after imaging.

Vasoconstriction by adrenaline and endothelin-1. To investigate the sensitivity of our prototype RSOM scanner and to demonstrate that fast and temporal vascular changes can be monitored, we used the short-acting vasoconstrictors adrenaline (L-adrenaline; B1337, ApexBio) and endothelin-1 (E7764, Sigma-Aldrich). Shaved BALB/c mice with CT26 tumours, as described above, were used for this study ($n = 3$ for each vasoconstrictor). First, a tail-vein catheter was inserted to enable rapid consecutive image acquisition without removing the mouse from the RSOM scanner. The tumour was imaged before as well as 1 min, 5 min and 10 min after injection of either 4 mg kg⁻¹ adrenaline (in 10% DMSO; D2650, Sigma-Aldrich) or 0.5 µg endothelin-1 (in 100 µl sodium chloride solution; BP358-1, Thermo Fisher Scientific). As a comparison, the contralateral side of the mouse without tumour was imaged over the same period of time after vasoconstrictor injection. No laser illumination was applied for this experiment. MIP images were analysed by measuring the diameter of several representative vessels in tumours and skin over time by drawing a straight line from one side of the respective vessel to the other side using ImageJ (Fiji), and measuring the vessel diameter over time after vasoconstrictor injection relative to the diameter before injection. Here, the vessel diameter correlates with the emitted ultrasound frequencies with smaller vessels emitting a range of higher frequencies and larger vessels emitting a range of lower frequencies as described above.

VTP with padeliporfin. Lyophilized palladium-bacteriochlorophyll derivative padeliporfin (Tookad soluble, formulated as padeliporfin di-potassium, also called WST11, Steba Biotech) was dissolved under light-protected conditions in sterile 5% dextran in water at 2 mg ml⁻¹ and stored at -20 °C. Before VTP, an aliquot was thawed and filtered through a syringe filter (0.2 µm). CT26 tumour-bearing mice were first infused through the tail vein with 9 mg kg⁻¹ of padeliporfin (not temperature controlled) for 5 min and the tumour was immediately illuminated using a diode laser (753 nm, Modulight) for 10 min at 120 mW cm⁻² (corresponding to a total light dose of 72 J cm⁻²). During illumination, skin around the tumour was covered with a black sheet to prevent treatment response in healthy tissue. Animals were imaged using RSOM before VTP and at multiple time points

afterwards for either short-term (5 min, 10 min, 30 min and 60 min; $n=3$) or long-term (1 h, 8 h, 18 h, 24 h, 30 h, 48 h, 3 d, 4 d and 5 d; $n=3$) monitoring of vascular changes. For the short-term imaging time points after VTP, the animals were kept in place for the entire time. For long-term imaging, the animals were removed after each scan from the RSOM and repositioned for each imaging session. For quantification, regions of interest were manually drawn on the MIP images using ImageJ, including only the tumour area and not the surrounding skin vessels. Longitudinal data were not coregistered, but were analysed separately. From RSOM images, the following parameters were analysed using ImageJ: haemoglobin signal, total vascular area and number of vessel fragments. The haemoglobin signal was calculated over time for each tumour by counting the pixels within the tumour area that were above a certain signal intensity for both smaller (green) and larger (red) vessels. Haemorrhage (diffuse signal in low frequencies) and clotted blood vessels (intense, dotted signal in both frequency ranges) were distinguished qualitatively within the images. The vascular area was also calculated within thresholded images and by measuring the area occupied by blood vessels within the tumour. Vessel fragments were quantified by counting the number of particles within thresholded RSOM images. No specific plugins were used. For all three parameters, the detected number before therapy was set to 100% and the following time points were calculated relative to before VTP. The same VTP treatment was performed for dual-wavelength RSOM imaging; oxygenation levels were determined before and at 5 min, 1 h and 24 h after VTP. Controls, such as animals with padeliporfin infusion or laser illumination only, were not included in this study as there are no expected changes of the tumour vessels as known from previous studies^{6,8,19}.

Comparison of the impact of VTP in xenografts derived from patients.

RSOM imaging was used to examine the vascular response and neoangiogenesis in tumour models that regressed or regrew after VTP. 5637 tumours ($n=11$) and UMUC3 tumours ($n=11$) were treated with VTP by retro-orbital injection of 9 mg kg^{-1} padeliporfin and 10 min of laser illumination at 150 mW cm^{-2} , delivered at 5 min after drug injection. Tumours were imaged before treatment and at 1 h, 24 h, 3 d, 7 d and 14 d after VTP and vascularization was analysed over time as described above ($n=3$ per tumour model). Simultaneously, throughout the duration of the experiment, tumour volume was measured in both tumour models using a digital calliper (1889-0600, Johnson) and the formula $V = \pi/6 \times (\text{length} \times \text{width} \times \text{height})$. Tumour volume after therapy was compared with the volume before VTP to determine the relative change over time.

Histological analysis. From mice euthanized at 1 h, 24 h, 5 d, 7 d and 14 d, excised tumour tissue samples were fixed in 4% paraformaldehyde (43368, Alfa Aesar) overnight at 4°C or, if tumours reached a size of more than 1 cm as in control mice, at room temperature to ensure complete fixation. Tissue samples were then washed three times in water and stored until further processing in 70% ethanol (459836, Sigma-Aldrich). After embedding in paraffin (39601006, Leica Biosystems), the tumours were cut into $10 \mu\text{m}$ slices and stained using haematoxylin (26381-02, Electron Microscopy Sciences) and eosin (HT110216, Sigma-Aldrich) for general tissue staining, antibodies against CD31 (Dianova, DIA-310, $2 \mu\text{g ml}^{-1}$) for endothelial cells and, therefore, blood vessels, and terminal deoxynucleotidyl transferase dUTP nick-end labelling (TUNEL; 11093070910, Sigma-Aldrich) to detect apoptotic cells. Staining was performed by the MSK Cytology Core facility following established protocols. The tissue slices were scanned using a high-resolution digital slide scanner (Pannoramic 250, 3DHistech).

Statistics. Data are indicated as mean \pm s.d or s.e.m. if not otherwise specified. Values were collected in Microsoft Excel and compared using unpaired two-tailed Student's *t*-tests with GraphPad Prism v.6.01. A *P* value of 0.05 or less was considered to be statistically significant.

Reporting Summary. Further information on research design is available in the Nature Research Reporting Summary linked to this article.

Data availability

The authors declare that all data from this study are available within the Article and its Supplementary Information. Raw data for the individual measurements are available on reasonable request.

Received: 10 December 2018; Accepted: 6 February 2020;

Published online: 12 March 2020

References

- Lin, Z., Zhang, Q. & Luo, W. Angiogenesis inhibitors as therapeutic agents in cancer: challenges and future directions. *Eur. J. Pharmacol.* **793**, 76–81 (2016).
- Gunther, J. E. et al. Dynamic diffuse optical tomography for monitoring neoadjuvant chemotherapy in patients with breast cancer. *Radiology* **287**, 778–786 (2018).
- Madar-Balakirski, N. et al. Permanent occlusion of feeding arteries and draining veins in solid mouse tumors by vascular targeted photodynamic therapy (VTP) with Tookad. *PLoS ONE* **5**, e10282 (2010).
- Goldschmidt, R., Vyacheslav, K. & Scherz, A. Real time laser speckle imaging monitoring vascular targeted photodynamic therapy. In *Optical Methods for Tumor Treatment and Detection: Mechanisms and Techniques in Photodynamic Therapy* (eds Kessel, D. H. & Hasan, T.) XXVI (SPIE, 2017).
- Gross, S., Gilead, A., Scherz, A., Neeman, M. & Salomon, Y. Monitoring photodynamic therapy of solid tumors online by BOLD-contrast MRI. *Nat. Med.* **9**, 1327–1331 (2003).
- Fleshker, S., Preise, D., Kalchenko, V., Scherz, A. & Salomon, Y. Prompt assessment of WST11-VTP outcome using luciferase transfected tumors enables second treatment and increase in overall therapeutic rate. *Photochem. Photobiol.* **84**, 1231–1237 (2008).
- Cornelis, F. H. et al. Contrast enhanced ultrasound imaging can predict vascular-targeted photodynamic therapy induced tumor necrosis in small animals. *Photodiagn. Photodyn. Ther.* **20**, 165–168 (2017).
- Neuschmelting, V. et al. WST11 vascular targeted photodynamic therapy effect monitoring by multispectral optoacoustic tomography (MSOT) in mice. *Theranostics* **8**, 723–734 (2018).
- Johnson, S. P., Ogunlade, O., Lythgoe, M. F., Beard, P. & Pedley, R. B. Longitudinal photoacoustic imaging of the pharmacodynamic effect of vascular targeted therapy on tumors. *Clin. Cancer Res.* **25**, 7436–7447 (2019).
- Ntziachristos, V. & Razansky, D. Molecular imaging by means of multispectral optoacoustic tomography (MSOT). *Chem. Rev.* **110**, 2783–2794 (2010).
- Taruttis, A. & Ntziachristos, V. Advances in real-time multispectral optoacoustic imaging and its applications. *Nat. Photonics* **9**, 219–227 (2015).
- Aguirre, J. et al. Precision assessment of label-free psoriasis biomarkers with ultra-broadband optoacoustic mesoscopy. *Nat. Biomed. Eng.* **1**, 0068 (2017).
- Omar, M., Schwarz, M., Soliman, D., Symvoulidis, P. & Ntziachristos, V. Pushing the optical imaging limits of cancer with multi-frequency-band raster-scan optoacoustic mesoscopy (RSOM). *Neoplasia* **17**, 208–214 (2015).
- Omar, M. et al. Optical imaging of post-embryonic zebrafish using multi orientation raster scan optoacoustic mesoscopy. *Light Sci. Appl.* **6**, e16186 (2017).
- Aguirre, J. et al. Broadband mesoscopic optoacoustic tomography reveals skin layers. *Opt. Lett.* **39**, 6297–6300 (2014).
- Schwarz, M., Omar, M., Buehler, A., Aguirre, J. & Ntziachristos, V. Implications of ultrasound frequency in optoacoustic mesoscopy of the skin. *IEEE Trans. Med. Imaging* **34**, 672–677 (2015).
- Berezhnoi, A. et al. Assessing hyperthermia-induced vasodilation in human skin in vivo using optoacoustic mesoscopy. *J. Biophotonics* **11**, e201700359 (2018).
- Schwarz, M., Buehler, A., Aguirre, J. & Ntziachristos, V. Three-dimensional multispectral optoacoustic mesoscopy reveals melanin and blood oxygenation in human skin in vivo. *J. Biophotonics* **9**, 55–60 (2015).
- Mazor, O. et al. WST11, a novel water-soluble bacteriochlorophyll derivative; cellular uptake, pharmacokinetics, biodistribution and vascular-targeted photodynamic activity using melanoma tumors as a model. *Photochem. Photobiol.* **81**, 342–351 (2005).
- Brandis, A. et al. Novel water-soluble bacteriochlorophyll derivatives for vascular-targeted photodynamic therapy: synthesis, solubility, phototoxicity and the effect of serum proteins. *Photochem. Photobiol.* **81**, 983–993 (2005).
- Azzouzi, A. R. et al. TOOKAD[®] soluble focal therapy: pooled analysis of three phase II studies assessing the minimally invasive ablation of localized prostate cancer. *World J. Urol.* **33**, 945–953 (2015).
- Noweski, A. et al. Medium-term follow-up of vascular-targeted photodynamic therapy of localized prostate cancer using TOOKAD soluble WST-11 (phase II trials). *Eur. Urol. Focus* **5**, 1022–1028 (2018).
- Taneja, S. S. et al. Final results of a phase I/II multicenter trial of WST11 vascular targeted photodynamic therapy for hemi-ablation of the prostate in men with unilateral low risk prostate cancer performed in the United States. *J. Urol.* **196**, 1096–1104 (2016).
- Ashur, I. et al. Photocatalytic generation of oxygen radicals by the water-soluble bacteriochlorophyll derivative WST11, noncovalently bound to serum albumin. *J. Phys. Chem. A* **113**, 8027–8037 (2009).
- Durand, R. E. Intermittent blood flow in solid tumours—an under-appreciated source of ‘drug resistance’. *Cancer Metastasis Rev.* **20**, 57–61 (2001).
- Morikawa, S. et al. Abnormalities in pericytes on blood vessels and endothelial sprouts in tumors. *Am. J. Pathol.* **160**, 985–1000 (2002).
- Rahbari, N. N. et al. Anti-VEGF therapy induces ECM remodeling and mechanical barriers to therapy in colorectal cancer liver metastases. *Sci. Transl. Med.* **8**, 360ra135 (2016).
- Jain, R. K. Antiangiogenesis strategies revisited: from starving tumors to alleviating hypoxia. *Cancer Cell* **26**, 605–622 (2014).
- Hernandez-Agudo, E. et al. Monitoring vascular normalization induced by antiangiogenic treatment with ¹⁸F-fluoromisonidazole-PET. *Mol. Oncol.* **10**, 704–718 (2016).
- Yang, J. et al. MR imaging biomarkers evaluating vascular normalization window after anti-vessel treatment. *Oncotarget* **9**, 11964–11976 (2018).

31. Biel, N. M., Lee, J. A., Sorg, B. S. & Siemann, D. W. Limitations of the dorsal skinfold window chamber model in evaluating anti-angiogenic therapy during early phase of angiogenesis. *Vasc. Cell* **6**, 17 (2014).
32. Kimm, S. Y. et al. Nonthermal ablation by using intravascular oxygen radical generation with WST11: dynamic tissue effects and implications for focal therapy. *Radiology* **281**, 109–118 (2016).
33. Mallidi, S., Watanabe, K., Timerman, D., Schoenfeld, D. & Hasan, T. Prediction of tumor recurrence and therapy monitoring using ultrasound-guided photoacoustic imaging. *Theranostics* **5**, 289–301 (2015).
34. Wang, H. W. et al. Treatment-induced changes in tumor oxygenation predict photodynamic therapy outcome. *Cancer Res.* **64**, 7553–7561 (2004).
35. Jathoul, A. P. et al. Deep in vivo photoacoustic imaging of mammalian tissues using a tyrosinase-based genetic reporter. *Nat. Photonics* **9**, 239–246 (2015).
36. He, H. et al. Capsule optoacoustic endoscopy for esophageal imaging. *J. Biophotonics* **12**, e201800439 (2019).
37. Haedicke, K. et al. Sonophore labeled RGD: a targeted contrast agent for optoacoustic imaging. *Photoacoustics* **6**, 1–8 (2017).
38. Caballero, M. A. A. *Incorporating Sensor Properties in Optoacoustic Imaging*. PhD thesis, Technical Univ. Munich (2013).

Acknowledgements

We thank N. Fan of the MSKCC Molecular Cytology Core Facility for assistance with histology; Y. Romin for support and feedback on image analysis; and D. Yarin of the MSKCC Molecular Cytology Core Facility for immunohistochemistry. This study was funded by the Thompson Family Foundation (Wade F. B. Thompson grant to J.C., A.S. and J.G.) and the National Cancer Institute (grant no. R01 CA212379 to J.G.). The study was also supported in part by the European grant INNODERM (no. 687866) Horizon 2020. We acknowledge P. Zanzonico and V. Ann Longo of the Small Animal Imaging Core Facility of MSKCC for their support (the Core is funded by the NIH Cancer Centre Support grant no. P30 CA008748).

Author contributions

K.H. designed and performed all of the experiments, processed and analysed the RSOM data, evaluated histological sections and wrote the manuscript. L.A. performed the VTP experiments in CT26 tumours and provided practical input for study planning and performance. M.O. developed the RSOM system, supplied technical input and performed the dual-wavelength RSOM measurements and analysis. A.B. conducted the dual-wavelength RSOM experiments and analysis. S.R. and M.S. conducted the craniotomy and performed the imaging of the mouse brain. K.N. performed the VTP experiments in bladder tumour models and supported RSOM imaging. H.-T.H. performed the VTP experiments in bladder tumour models and supported histological analysis with C.L.-M. K.K. provided conceptual input and designed the experiments in bladder tumour models. T.R. provided input for the design of the brain experiments. J.C. provided input and designed the VTP experiments. V.N. provided technical input for RSOM imaging and supervised the dual-wavelength measurements. A.S. supervised the VTP experiments, provided conceptual input and designed the experiments. J.G. supervised the study, provided input for all of the experiments and the study concept, and edited the paper.

Competing interests

V.N. is a shareholder in iThera Medical GmbH in Munich, Germany, which produces a commercial version of the monospectral RSOM (not used in this study). A.S. is an inventor of padeliporfin and has a financial interest from licensing fees.

Additional information

Supplementary information is available for this paper at <https://doi.org/10.1038/s41551-020-0527-8>.

Correspondence and requests for materials should be addressed to J.G.

Reprints and permissions information is available at www.nature.com/reprints.

Publisher's note Springer Nature remains neutral with regard to jurisdictional claims in published maps and institutional affiliations.

© The Author(s), under exclusive licence to Springer Nature Limited 2020

Reporting Summary

Nature Research wishes to improve the reproducibility of the work that we publish. This form provides structure for consistency and transparency in reporting. For further information on Nature Research policies, see [Authors & Referees](#) and the [Editorial Policy Checklist](#).

Statistics

For all statistical analyses, confirm that the following items are present in the figure legend, table legend, main text, or Methods section.

n/a Confirmed

- | | | |
|-------------------------------------|-------------------------------------|--|
| <input type="checkbox"/> | <input checked="" type="checkbox"/> | The exact sample size (n) for each experimental group/condition, given as a discrete number and unit of measurement |
| <input type="checkbox"/> | <input checked="" type="checkbox"/> | A statement on whether measurements were taken from distinct samples or whether the same sample was measured repeatedly |
| <input type="checkbox"/> | <input checked="" type="checkbox"/> | The statistical test(s) used AND whether they are one- or two-sided <i>Only common tests should be described solely by name; describe more complex techniques in the Methods section.</i> |
| <input checked="" type="checkbox"/> | <input type="checkbox"/> | A description of all covariates tested |
| <input checked="" type="checkbox"/> | <input type="checkbox"/> | A description of any assumptions or corrections, such as tests of normality and adjustment for multiple comparisons |
| <input type="checkbox"/> | <input checked="" type="checkbox"/> | A full description of the statistical parameters including central tendency (e.g. means) or other basic estimates (e.g. regression coefficient) AND variation (e.g. standard deviation) or associated estimates of uncertainty (e.g. confidence intervals) |
| <input type="checkbox"/> | <input checked="" type="checkbox"/> | For null hypothesis testing, the test statistic (e.g. F , t , r) with confidence intervals, effect sizes, degrees of freedom and P value noted <i>Give P values as exact values whenever suitable.</i> |
| <input checked="" type="checkbox"/> | <input type="checkbox"/> | For Bayesian analysis, information on the choice of priors and Markov chain Monte Carlo settings |
| <input checked="" type="checkbox"/> | <input type="checkbox"/> | For hierarchical and complex designs, identification of the appropriate level for tests and full reporting of outcomes |
| <input checked="" type="checkbox"/> | <input type="checkbox"/> | Estimates of effect sizes (e.g. Cohen's d , Pearson's r), indicating how they were calculated |

Our web collection on [statistics for biologists](#) contains articles on many of the points above.

Software and code

Policy information about [availability of computer code](#)

Data collection

The data were collected with an RSOM prototype, by using a Matlab-based software made only for this prototype device.

Data analysis

The data were analysed by using Microsoft Excel and GraphPad Prism Version 6.01. For image presentation and quantification, ImageJ (Fiji) was used.

For manuscripts utilizing custom algorithms or software that are central to the research but not yet described in published literature, software must be made available to editors/reviewers. We strongly encourage code deposition in a community repository (e.g. GitHub). See the Nature Research [guidelines for submitting code & software](#) for further information.

Data

Policy information about [availability of data](#)

All manuscripts must include a [data availability statement](#). This statement should provide the following information, where applicable:

- Accession codes, unique identifiers, or web links for publicly available datasets
- A list of figures that have associated raw data
- A description of any restrictions on data availability

The authors declare that all data from this study are available in the paper and its Supplementary Information. Raw data for the individual measurements are available on reasonable request.

Field-specific reporting

Please select the one below that is the best fit for your research. If you are not sure, read the appropriate sections before making your selection.

- Life sciences Behavioural & social sciences Ecological, evolutionary & environmental sciences

For a reference copy of the document with all sections, see [nature.com/documents/nr-reporting-summary-flat.pdf](https://www.nature.com/documents/nr-reporting-summary-flat.pdf)

Life sciences study design

All studies must disclose on these points even when the disclosure is negative.

| | |
|-----------------|---|
| Sample size | No a priori power analysis was performed. |
| Data exclusions | No data were excluded from the analyses. |
| Replication | To verify the reproducibility of the experimental findings, 3 mice were used for each experimental setup, and analysis was performed on several tumors or blood vessels. There are no doubts that the results are reproducible as experiments were performed on several days. |
| Randomization | Mice were randomly selected for different treatment groups and tumor implantation. For the treatment experiments, mice with sufficiently sized tumors were selected from a cohort of animals. |
| Blinding | Blinding was not relevant to the study, as all mice were treated with therapy and analysed for the whole-tumor signal rather than for selected areas. |

Reporting for specific materials, systems and methods

We require information from authors about some types of materials, experimental systems and methods used in many studies. Here, indicate whether each material, system or method listed is relevant to your study. If you are not sure if a list item applies to your research, read the appropriate section before selecting a response.

Materials & experimental systems

| n/a | Involvement in the study |
|-------------------------------------|---|
| <input type="checkbox"/> | <input checked="" type="checkbox"/> Antibodies |
| <input type="checkbox"/> | <input checked="" type="checkbox"/> Eukaryotic cell lines |
| <input checked="" type="checkbox"/> | <input type="checkbox"/> Palaeontology |
| <input type="checkbox"/> | <input checked="" type="checkbox"/> Animals and other organisms |
| <input checked="" type="checkbox"/> | <input type="checkbox"/> Human research participants |
| <input checked="" type="checkbox"/> | <input type="checkbox"/> Clinical data |

Methods

| n/a | Involvement in the study |
|-------------------------------------|---|
| <input checked="" type="checkbox"/> | <input type="checkbox"/> ChIP-seq |
| <input checked="" type="checkbox"/> | <input type="checkbox"/> Flow cytometry |
| <input checked="" type="checkbox"/> | <input type="checkbox"/> MRI-based neuroimaging |

Antibodies

| | |
|-----------------|---|
| Antibodies used | Antibodies were used from the MSK Cytology Core facility for histological staining of H&E, CD31 and TUNEL. Established protocols were used. |
| Validation | For each staining, an isotype control was additionally performed, which was always negative in the staining outcome. |

Eukaryotic cell lines

Policy information about [cell lines](#)

| | |
|--|---|
| Cell line source(s) | CT26, 5637 and UMUC3 cells were purchased from ATCC. |
| Authentication | All cell lines have been confirmed as authentic through short tandem repeats. |
| Mycoplasma contamination | The cell lines were not tested for mycoplasma contamination in direct connection to this study. However, testing on a regular basis is performed in the lab for each cell line. |
| Commonly misidentified lines (See ICLAC register) | There were no misidentified cell lines. |

Animals and other organisms

Policy information about [studies involving animals](#); [ARRIVE guidelines](#) recommended for reporting animal research

Laboratory animals

Female BALB/c mice (Taconic, 6–8 weeks old, 20–28 g); male NSG mice (NOD.Cg-Prkdcscid Il2rgtm1Wjl/SzJ, Jackson Laboratory, 6–8 weeks old, 20–28 g)

Wild animals

The study did not involve wild animals.

Field-collected samples

The study did not involve samples collected from the field.

Ethics oversight

All animal procedures were approved by the Institutional Animal Care and Use Committee (IACUC), and followed institutional and NIH guidelines.

Note that full information on the approval of the study protocol must also be provided in the manuscript.